

Cold-formed austenitic stainless steel SHS brace members under cyclic loading: finite element modelling, design considerations

YongHyun Cho^a, Fangying Wang^b, and TaeSoo Kim^{*}

^a*Sustainable Building Research Center, Hanyang University, Ansan 15588, Republic of Korea*

^b*Department of Civil Engineering, University of Nottingham, Nottingham NG7 2RD, United Kingdom*

^{*}*School of Architecture and Architectural Engineering, Hanyang University, Ansan 15588, Republic of Korea*

Abstract. This study presents a numerical investigation into the hysteretic behavior of cold-formed austenitic stainless steel square hollow section (SHS) brace members using a commercial finite element (FE) analysis software ABAQUS/Standard. The initial/post buckling and fracture life of SHS brace members are comprehensively investigated through parametric studies with FE models incorporating ductile fracture model, which is validated against the existing laboratory test results collected from the literature. It is found that the current predictive models are applicable for the initial buckling strengths of SHS brace members under cyclic loading, while result in significant inaccuracy in predictions for the post-buckling strength and fracture life. The modified predictive model is therefore proposed and the applicability was then confirmed through excellent comparisons with test results for cold-formed austenitic stainless SHS brace members.

Keywords: austenitic stainless steel; brace; square hollow section; buckling; fracture life; seismic design; hysteretic behavior

1. Introduction

Hollow structural section (HSS) braces have been extensively used for lateral force resisting systems in steel building frame structures, owing primary to combined advantages of large flexural rigidity and compression capacity and low fabrication cost. In the concentrically braced frames (CBFs), the brace plays a pivotal role in absorbing seismic energy by yielding in tension and buckling in compression, thereby reducing the forces in other framing members. The braces should be designed to exhibit adequate inelastic deformation capacity prior to fracture under seismic loading. Cold-formed HSS features relatively smaller thickness and overall sizes compared to hot-rolled sections, therefore, in some cases it is difficult to satisfy large seismic capacity requirement. The difficulty is addressed by using the stainless steel HSS as backup since it has a larger level of ductility and strain hardening than the conventional carbon steel counterpart (Zhou et al. 2018; Wang et al. 2020; Zhou et al. 2022). It is reported that stainless steel brace members are able to sustain more cycles of loading than the carbon steel prior to fracture (Nip et al. 2010a). In addition, the high quality of fire and corrosion resistance of stainless steel is beneficial for structures exposed to aggressive environmental condition. The presence of the chromium oxide layer eliminates the need for maintenance during its service life.

However, from the structural engineering point of view, the use of stainless steel may not be suitable for the

construction of whole structures due to their high initial material cost, which is generally equivalent to 4~5 times that of carbon steel. In light of this, development of structural design rules for stainless steel is imperative to achieve a more economical and sustainable design that eliminates material wastes.

Since the first design manual for structural stainless steel, the AISI specification for the Design of Light Gage Cold-Formed Stainless Steel Structural Members published in 1968 (AISI 1968), various international design codes have been available and regularly revised. Nevertheless, to date, there is no design code for seismic design of stainless steel structures. Basically, stainless steel specimens had greater extent of cyclic hardening capacity and more sensitive to the cold-forming effect in comparison to the carbon steel ones (Nip et al. 2010b). The suitability of the hysteretic model developed based on carbon steel for stainless steel remains unsolved.

Although studies of the cold-formed stainless steel square and rectangular hollow section (SHS and RHS) under static loading have been extensively reported by many researchers (Liu & Young 2003; Ahmed & Ashraf 2017), studies and data on their hysteretic behavior under cyclic loading are still scarce (Fang et al. 2018; Zheng et al. 2022). Nip et al. (2010a) presented test and numerical data of carbon steel and stainless steel tubular bracing members, and found that stainless steel possesses longer fracture life and greater

*Corresponding author, Ph.D. Professor,
E-mail: tskim0709@hanyang.ac.kr

^aPh.D., Postdoctoral Fellow

^bPh.D., Assistant Professor

^cPh.D., Associate Professor

Table 1 Measured geometric properties of SHS brace specimens

Specimen	H (mm)	B (mm)	t (mm)	L (mm)	λ_c	λ_s	Section classification	Δ_y (mm)
STS304 - 50 × 50 × 3 × 0.8	50.07	50.07	3.06	800	0.42	21.92	Class 1	3.26
STS304 - 50 × 50 × 3 × 1.8	50.24	49.92	3.05	1797	0.84	22.00	Class 1	6.53
STS304 - 70 × 70 × 3 × 0.8	70.20	69.79	3.07	800	0.29	30.73	Class 1	2.67
STS304 - 70 × 70 × 3 × 1.8	70.12	70.02	3.01	1797	0.57	31.44	Class 1	5.35
STS316 - 50 × 50 × 3 × 0.8	50.11	47.62	3.06	800	0.42	20.72	Class 1	2.70
STS316 - 50 × 50 × 3 × 1.8	50.06	49.89	3.04	1800	0.82	21.42	Class 1	5.40
STS316 - 70 × 70 × 3 × 0.8	69.83	69.88	3.02	799	0.26	28.18	Class 1	2.23
STS316 - 70 × 70 × 3 × 1.8	69.89	69.97	3.04	1799	0.52	28.01	Class 1	4.47

* Δ_y is yield displacement (LF_y/E)

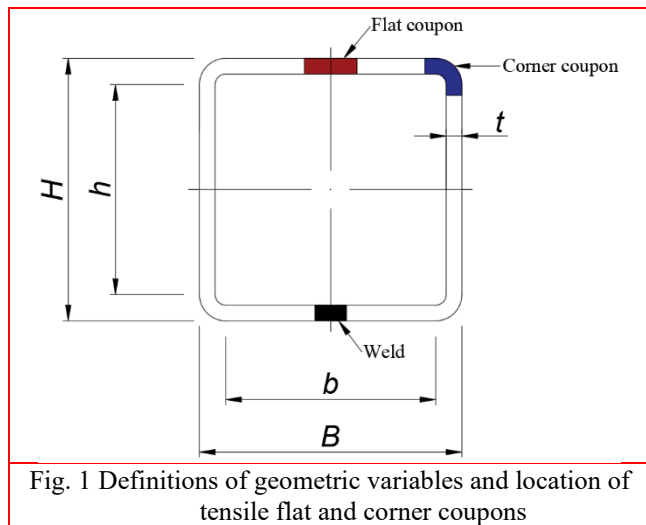


Fig. 1 Definitions of geometric variables and location of tensile flat and corner coupons

dissipative energy that are desirable properties for seismic design.

Zhou et al. (2018) pointed out that the empirical model of Trembly (2002) for prediction of post-buckling resistance, which is derived from the results of the carbon steel specimens is inaccurate for the stainless steel specimens. More recently, Kim et al. (2021) developed a laboratory test program to investigate the hysteretic behavior of cold-formed stainless steel SHS brace members under cyclic axial loading. All the specimens were made of two different austenitic stainless steels and one duplex stainless steel. It was found that the current codified design equations produced underestimated predictions for the buckling strengths of brace members.

Finite element analysis is a powerful tool to understand experimentally observed phenomenon, as it can provide the stress/strain contours. In order to gain better insight into the hysteretic behavior of cold-formed austenitic stainless steel SHS braces, finite element simulation procedure is developed as described in this paper and validated against the laboratory test results reported by the corresponding author (Kim et al. 2021). Subsequently, the validated FE model is herein employed to generate more databank. This parametric study allows further investigation on the effects of global and local slenderness ratios on the initial/post-buckling strengths and fracture life. The applicability of existing design codes

and predictive models, derived from the results of carbon steel specimens, are assessed based on the results of the parametric study. From here, a new model for predicting fracture life is proposed.

2. Overview of cyclic test of austenitic stainless steel SHS braces

The laboratory test program conducted by Kim et al. (2021) includes eight stainless steel SHS brace specimens, the results of which were used to develop and validate the Finite Element (FE) models described in the present work. The SHS specimens were fabricated from two types of austenitic stainless steel plates, namely STS304 TKC (corresponds to EN 1.4301 and AISI 304) and STS316 TKC (corresponds to EN 1.4401 and AISI 316) in KS D 3536 (KS 2015). The geometric variables of SHS brace specimens are defined in Fig. 1, in which H and B are the over depth and width, respectively; t is the section thickness. Buckling behavior of SHS brace members subjected to cyclic loading is mainly associated with the global slenderness λ_c and the local slenderness λ_s as defined by:

$$\lambda_c = \sqrt{F_y A_s / N_{cr}} \quad (1)$$

$$\lambda_s = b / t \varepsilon \quad (2)$$

where F_y = yield stress; A_s = gross cross-section area; N_{cr} = elastic critical buckling load; $\varepsilon = (235E / 210000F_y)^{0.5}$; and b = flat width of relevant plate element.

Table 1 lists the measured geometric properties and the cross-section classification of all the brace specimens used in the test program. It should be noticed that the cross-sections of all the specimens are classified as Class 1 in accordance with the Eurocode 3 part 1-4 (Eurocode 2015). It is well known that the steel material in the corner region features higher yield stress but lower ductility than the flat material due to cold-working (Ashraf et al. 2005). The longitudinal flat and corner tensile coupons were extracted from the three non-welded sides of SHS employed in the bracing tests. The tension coupon tests were conducted under displacement

Table 2 Average material properties

Specimen	t (mm)	E (GPa)	F_y (MPa)	F_u (MPa)	F_u/F_y	ϵ_f (%)
STS304 - 50 × 50 × 3 - Flat	3.01	203	529	785	1.48	49.3
STS304 - 50 × 50 × 3 - Corner	3.14	196	663	867	1.31	44.8
STS304 - 70 × 70 × 3 - Flat	2.98	183	447	710	1.59	55.0
STS304 - 70 × 70 × 3 - Corner	3.26	222	864	1144	1.32	46.8
STS316 - 50 × 50 × 3 - Flat	3.01	199	490	627	1.28	42.9
STS316 - 50 × 50 × 3 - Corner	3.16	154	520	670	1.29	38.0
STS316 - 70 × 70 × 3 - Flat	2.99	208	414	623	1.51	51.5
STS316 - 70 × 70 × 3 - Corner	3.15	161	539	714	1.32	38.7

Table 3 Summary of test results (Kim et al. 2021)

Specimen	Number of cycles (Δ/Δ_y) to:				$N_{b,Test}$ (kN)	$N_{t,Test}$ (kN)	E_{total} (kJ)
	N_{GB}	N_{LB}	N_{CO}	N_{TF}			
STS304 - 50 × 50 × 3 × 0.8	10 (2.0)	-	-	18 (4.0)	336	355	39
STS304 - 50 × 50 × 3 × 1.8	7 (1.0)	-	-	16 (4.0)	218	356	38
STS304 - 70 × 70 × 3 × 0.8	10 (2.0)	10 (2.0)	13 (3.0)	26 (4.0)	461	380	68
*STS304 - 70 × 70 × 3 × 1.8	-	-	10 (2.0)	10 (2.0)	360	307	8
STS316 - 50 × 50 × 3 × 0.8	10 (2.0)	13 (3.0)	-	34 (4.0)	289	327	82
STS316 - 50 × 50 × 3 × 1.8	13 (3.0)	17 (4.0)	-	27 (4.0)	204	306	65
STS316 - 70 × 70 × 3 × 0.8	16 (4.0)	16 (4.0)	16 (4.0)	42 (4.0)	417	353	100
STS316 - 70 × 70 × 3 × 1.8	10 (2.0)	10 (2.0)	-	21 (4.0)	335	387	62

*Failed by weld fracture of jig

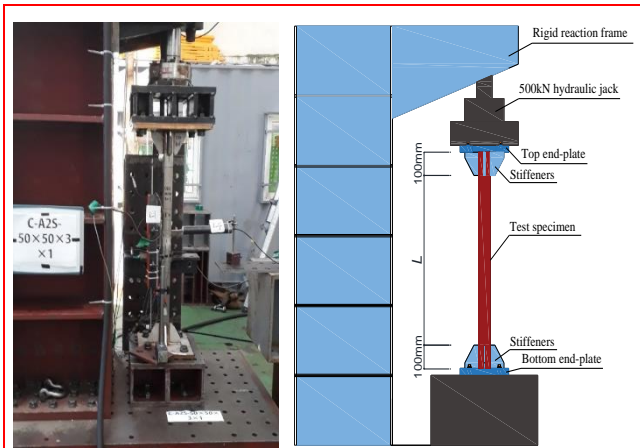


Fig. 2 Test set-up used in the work of Kim et al. (2021)

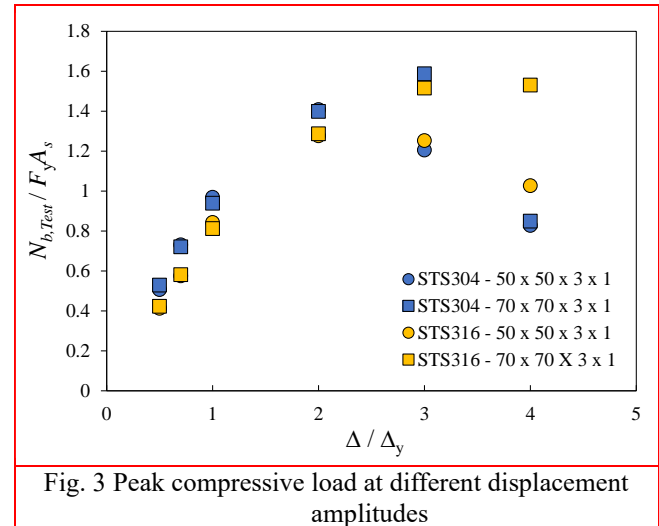


Fig. 3 Peak compressive load at different displacement amplitudes

control in accordance with Section 7 of ASTM E8-16 (ASTM 2016).

The average material properties including thickness t , elastic modulus E , yield (0.2% proof) stress F_y , tensile strength F_u and elongation at fracture ϵ_f are summarised in Table 2. Fig. 2 illustrates the details of test set-up of brace assembly in the loading frame. A 500 kN hydraulic actuator was used to apply a cyclic axial load on brace specimens by means of displacement control. The applied load was recorded with the load cell of the actuator, while the axial displacement was recorded through pre-calibrated cable-

extension transducers (CETs). The incremental cyclic loading protocol was described in accordance with ATC-24 (ATC 1992) for the cyclic testing of structural steel components.

The numbers of cycles to global buckling N_{GB} , local buckling N_{LB} , corner opening N_{CO} and throughout fracture N_{TF} for each specimen are listed in Table 3. It can be seen from Table 3 that the smaller global slenderness postponed the occurrence of global buckling. The largest N_{GB} was achieved by Specimen STS316 – 70 × 70 × 3 × 0.8 with the smallest value of λ_c among the tested specimens. The fracture life was directly dependent on both global and local

Table 4 Validation of FE models

Specimen	Imperfection		Buckling load (kN)			Tensile resistance (kN)		
	Global	Local	$N_{b,Test}$	$N_{b,FEA}$	$N_{b,FEA}/N_{b,Test}$	$N_{t,Test}$	$N_{t,FEA}$	$N_{t,FEA}/N_{t,Test}$
STS304 - 50 × 50 × 3 × 0.8	L/1000	t/10	336	339	1.01	355	368	1.04
STS304 - 50 × 50 × 3 × 1.8			218	226	1.04	356	367	1.03
STS304 - 70 × 70 × 3 × 0.8	L/3000	t/500	461	400	0.87	380	431	1.13
*STS304 - 70 × 70 × 3 × 1.8			360	-	-	307	-	-
STS316 - 50 × 50 × 3 × 0.8	L/500	t/10	289	322	1.12	327	348	1.06
STS316 - 50 × 50 × 3 × 1.8			204	213	1.05	306	343	1.12
STS316 - 70 × 70 × 3 × 0.8	L/2000	t/500	417	366	0.88	353	380	1.08
STS316 - 70 × 70 × 3 × 1.8			335	324	0.97	387	389	0.98
Mean					0.99			1.06
COV					0.085			0.047

*Failed by weld fracture of jig

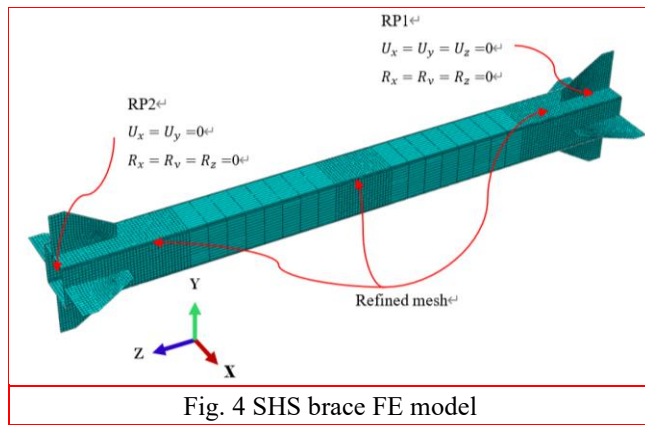


Fig. 4 SHS brace FE model

(cross-sectional) slenderness.

The shorter member length, the stockier section size, consequently the higher number of cycles before fracture. In general, larger level of material ductility tended to delay the fracture occurrence. However, a greater number of cycles to throughout fracture N_{TF} were obtained in STS316 specimens than their STS304 counterparts, even though the former had higher yield stress and ductility level than the latter one, as reported in Table 2.

It can be also seen from Fig. 3 that STS304 specimens exhibits more pronounced reduction in compressive resistance upon the onset of buckling. This phenomenon could be largely due to the strain-induced α' martensitic transformation (Chiu et al. 2005). With lower nickel equivalent, STS304 exhibited lower austenite stability than STS316. Thus, higher α' martensite volume fractions formed in STS304, which consequently lead to earlier occurrence of fatigue crack (Shrinivas et al. 1995; Sohrabi et al. 2020).

Table 3 lists the experimental buckling load $N_{b,Test}$ and the tensile resistance $N_{t,Test}$ of the tested bracing specimens. All the specimens reached $N_{b,Test}$ by global buckling. For a given section dimensions, the shorter specimens have a lower buckling load as they are more able

to postpone the occurrence of global buckling. The total accumulated energy dissipation E_{total} , which can be quantitatively determined by summing up the areas of all hysteresis loop, is also presented in Table 3. It is confirmed that the energy dissipation is closely associated with the flexural rigidity. STS304 specimens is found to have lower energy dissipation capacity than the comparable STS316 one due to early global buckling.

3. Non-linear finite element analysis

3.1 General description

In order to simulate non-linear buckling and post-buckling of SHS brace specimens, finite element models were developed using a commercial software ABAQUS/Standard (ABAQUS 2018). Note that Specimen STS304 – 70 × 70 × 3 × 1.8 was excluded herein due to the immature fracture mode (weld fracture in jig). A typical FE model of the brace specimen is displayed in Fig. 4. The geometric properties of FE model are consistent with those presented in Table 1. A general-purpose linear 4-sided shell elements with reduced integration (S4R) which have shown successful buckling simulation in the previous studies (Kumar & Sahoo 2018; Hassan et al. 2018), were used to model all the components in the brace assembly.

The number of elements, which directly control the computational time was minimized by adjusting mesh density in the model. Specifically, the finer meshed elements were used in the ends of stiffeners and mid-span where buckling occurrence was anticipated. The element size was 5 mm for the refined region, whilst a coarser mesh size of 30 mm was used for the rest of the model. Five integration points through the element thickness were considered to avoid hour glassing phenomenon. The total element number was approximately 13,744. Tie constraints were used to simulate the weld junction between stiffeners and brace member. Coupling constraints were used to couple the end

Table 5 Chaboche model parameters used in FE models

Specimen	$\sigma _0$ (MPa)	Q_∞ (MPa)	b	C_k (MPa)	γ_k
STS304 - 50 × 50 × 3 - Flat	531.9	218.4	0.22	2111.6	1.45
STS304 - 50 × 50 × 3 - Corner	729.0	283.2	0.25	1686.3	1.19
STS304 - 70 × 70 × 3 - Flat	518.7	172.3	0.25	1936.3	1.69
STS304 - 70 × 70 × 3 - Corner	115.8	244.9	0.17	1993.3	1.19
STS316 - 50 × 50 × 3 - Flat	463.9	197.3	1.27	1709.7	2.77
STS316 - 50 × 50 × 3 - Corner	729.0	283.2	0.25	1597.6	1.13
STS316 - 70 × 70 × 3 - Flat	428.1	288.7	1.25	1577.3	2.19
STS316 - 70 × 70 × 3 - Corner	611.4	107.0	0.74	1691.9	3.16

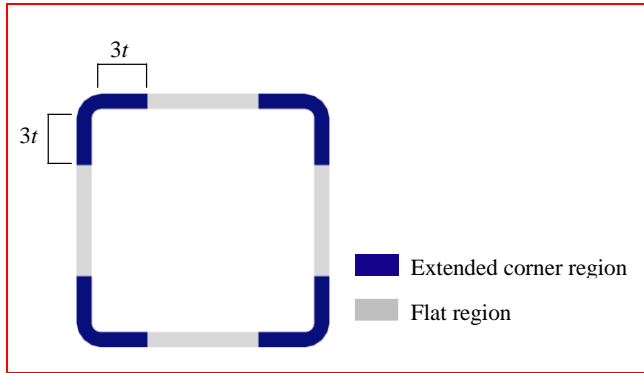


Fig. 5 Material properties assigned in SHS brace FE model

sections of the brace to reference points. The axial cyclic loading was applied by displacing reference point RP-2.

In addition, the effects of the initial geometric imperfections arising from fabrication and handling were incorporated into the present FE models by using *IMPERFECTION command. An elastic buckling analysis was conducted to obtain the lowest global and local eigenmodes, which were then assigned to the models to account for the possible instabilities of the brace members. Four amplitudes of global imperfection ($L/500$, $L/1000$, $L/2000$ and $L/3000$) and local imperfection ($t/10$, $t/100$, $t/300$ and $t/500$) were considered, and then the desirable one was taken as the scale factor to update the model coordinate. The combination of the global and local imperfection magnitude for each section are listed in Table 4.

3.2 Material modelling

To replicate the cyclic behavior of steel material, a combined isotropic/kinematic hardening model built in ABAQUS material library was employed. This model is developed based on the research work of Lemaitre and Chaboche (Lemaitre & Chaboche 1990). The expansion or contraction of the yield surface in the stress space is described by the isotropic hardening component, as expressed in Eq. (3).

$$\sigma_0 = \sigma|_0 + Q_\infty(1 - e^{-b\varepsilon^{pl}}) \quad (3)$$

where σ_0 = size of the yield surface; $\sigma|_0$ = initial yield stress; Q_∞ = maximum change in size of the yield surface;

b = rate of change of yield surface size as plastic strain increases; and ε^{pl} = equivalent plastic strain. On the other hand, the yield surface shift is described by the kinematic hardening component, which can be expressed as:

$$\alpha_k = C_k \frac{1}{\gamma_k} (1 - e^{-\gamma_k \varepsilon^{pl}}) + \alpha_{k,1} e^{-\gamma_k \varepsilon^{pl}} \quad (4)$$

where α_k = k th back stress; C_k = maximum change in back stress magnitude; γ_k = change rate of back stress as plastic strain increases. The allowance for the cold-forming effect on corner regions of SHS sections was made in the current FE model. As seen in Fig. 5, the corner material properties were assigned to the extended flat regions beyond the corner to a distance equal to three times the material thickness, whereas the flat material properties were assigned to the remainder of the sections, following the recommendations in (Ashraf et al. 2006; Ma et al. 2018; Tayyebi & Sun 2021). Cycling testing on materials needs to be conducted. However, this was not provided in the test programme reported in (Kim et al. 2021), therefore, Chaboche model parameters are calibrated against tension coupon data following the procedures proposed by Zub et al. (2019). The obtained parameters are listed in Table 5.

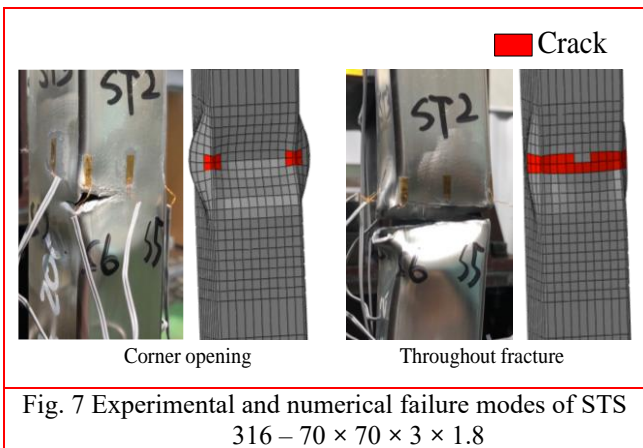
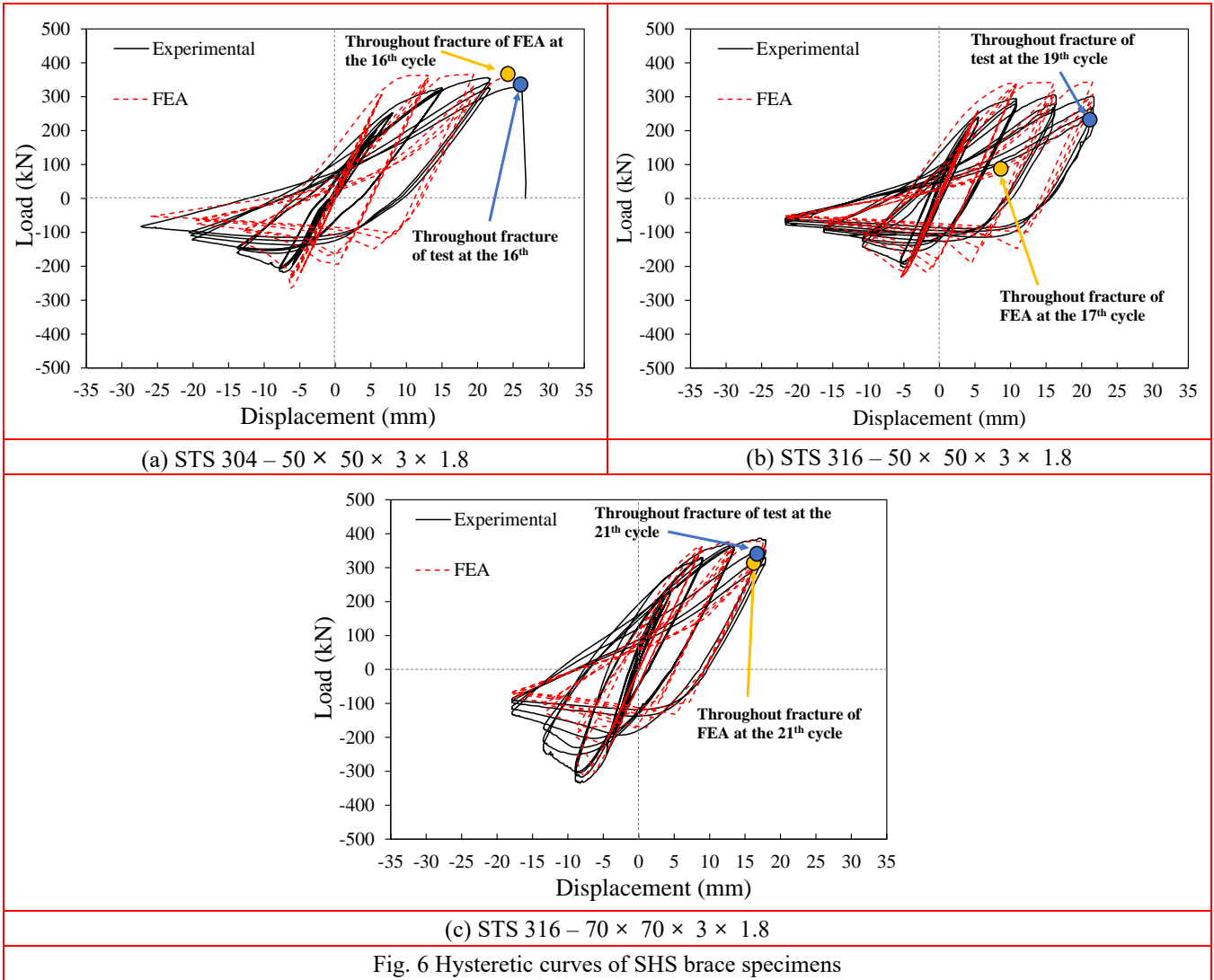
3.3 Ductile damage modelling

The Void Growth Model (VGM) (Rice & Tracey 1969) that considers micro-scale phenomenon such as nucleation, growth, and coalescence of voids has been adopted in the present FE models. This model defines the fracture equivalent plastic strain ε_f^{pl} as a function of stress triaxiality η as expressed in Eq. (5). Fracture of the element initiates once the damage index ω_f , as calculated by Eq. (6), reaches unity,

$$\varepsilon_f^{pl}(\eta) = \alpha \cdot \exp(-1.5 \cdot \eta) \quad (5)$$

$$\omega_f = \int \frac{d\varepsilon^{pl}}{\varepsilon_f^{pl}(\eta)} = 1 \quad (6)$$

where $\eta = p/q$; p = pressure stress; q = Mises equivalent stress; and ε^{pl} = equivalent plastic strain (PEEQ).



In general, tensile testing and finite element simulation of notched specimens are necessary to construct a fracture locus. However, given limited resources of the present work, the model parameter α for the present FE model is calibrated based on the results of the tested bracing specimens through the iteration process. During damage propagation, the element can become severely distorted,

which lead to impractical computation time. Therefore, damage evolution law was assumed to be 0.001 in terms of effective plastic displacement to achieve a sudden drop in the load after the damage onset, which is consistent with the approach used in previous simulation (Yang et al. 2021). In addition, the element was set to lose their material stiffness up to 90% to facilitate numerical convergence.

3.4 Validation of FE models

The comparisons between the test and FEA hysteretic responses are given in Fig. 6. A certain level of discrepancy between the predicted stiffness and that observed during testing is observed in Specimen STS304 – 50 × 50 × 3 × 1.8. This is probably attributed to the accidental error of CET measurement and the uncertainty related to the initial geometric imperfection. Nevertheless, by applying the framework described in the preceding section, the FE models are able to replicate the hysteretic response well for the majority of the SHS stainless steel brace specimens. It can be also observed that the fracture life (represented as cycles before fracture) predicted from FE simulation matches well with that obtained from tests.

Table 7 Evaluation of the different buckling curves codified in design specifications

Steel material	No. of tests	No. of FEA	$N_b/N_{b,EC3}$		$N_b/N_{b,AISC}$	
			Mean	COV	Mean	COV
STS304	3	45	1.00	0.066	0.97	0.086
STS316	4	45	0.98	0.091	0.96	0.100

Table 6 Parameter matrix

Parameters	Details
Stainless steel grade	STS304, STS316
Member length (mm)	2000, 2500, 3000, 3500, 4000
Tube wall thickness (mm)	2, 3, 4, 5, 6
Member section (mm)	50 × 50, 70 × 70
Total number of models	90

Overshoots on the compression side can be observed at the post-buckling stage, where the degradations of the compressive resistance are much more severe in the FE simulation than in the tests. This is most likely associated with the limited number of parameters in combined hardening model to account for the Bauschinger effect (Nip et al. 2010a; Haddad 2015).

The simulated local and global buckling modes are highly consistent with the test results, as shown in Fig. 7. The buckling load and tensile resistance obtained in the FE simulations and the tests are listed in Table 4, where $N_{b,FEA}$ and $N_{t,FEA}$ are the numerical buckling load and tensile resistance, respectively. Good agreement is achieved. The mean value of FE-to-test buckling load ($N_{b,FEA}/N_b$) and tensile resistance ($N_{t,FEA}/N_t$) are 0.99 and 1.06, respectively, with the corresponding coefficient of variation (COV) of 0.085 and 0.047. with the corresponding coefficient of variation (COV) of 0.085 and 0.047.

3.5 Parametric study

The validated FE model was utilized in the subsequent parametric studies to further investigate inelastic buckling response of braces with varying global and local slenderness ratios. The selected slenderness parameters are presented in Table 6. The overall cross-section dimensions used for the validation of the FE models remain unchanged, while the tube wall thickness is varied from 2 to 6 mm. In order to neglect the effect of local buckling prior to yielding, slender (Class 4) cross sections were not considered, which also aligns with the practical use of compact sections for brace members. Five different member lengths, from 2000 mm to 4000 mm with an increment of 500 mm, were selected, which results in the global slenderness ranging from 0.52 to 1.79. This indicates that all specimens used in the parametric studies would fail in inelastic flexural buckling as per AISC 370-21 specification (AISC 2021), which is confirmed through the FE outputs presented in the following section.

4. Design considerations

4.1 Initial buckling strength

Based on the Perry-Robertson formula, the European

code for stainless steels (Eurocode 2015; Eurocode 2020) provides the following equation for flexural buckling strength of stainless steel columns under axial compression.

$$N_{b,EC3} = \frac{\chi A_s F_y}{\gamma_{M1}} \quad (7)$$

$$\chi = \frac{1}{\phi + \sqrt{\phi^2 - \bar{\lambda}^2}} \leq 1 \quad (8)$$

$$\phi = 0.5[1 + \alpha(\lambda_c - \lambda_0) + \bar{\lambda}^2] \quad (9)$$

where χ = overall buckling reduction factor; A_s = gross cross-sectional area; and γ_{M1} = partial factor, which is assumed as unity for SHS used in the present work; ϕ = buckling coefficient; α = imperfection factor and λ_0 = non-dimensional limiting slenderness, which are taken as 0.49 and 0.30 conforming to the upcoming version of the prEN 1993-1-4:2020 (Eurocode 2020), instead of 0.4 codified in the 2015 edition (Eurocode 2015).

The revised version of the AISC 370-21 specification for Structural Stainless Steel Buildings (AISC 2021) has adopted a new design approach, which provides various buckling curves for compression members according to their cross-section type and stainless steel family with a transition between inelastic and elastic buckling responses, as shown in Eqs. (10-14),

$$N_{b,AISC} = A_s F_{cr} \quad (10)$$

$$F_{cr} = F_y \quad \text{for } \lambda_c \leq \beta_0 \quad (11)$$

$$F_{cr} = 1.2(\beta_1^{(\lambda_c)^\alpha}) F_y \quad \text{for } \beta_0 < \lambda_c \leq \lambda_{lim} \quad (12)$$

$$F_{cr} = \beta_2 F_{cr} \quad \text{for } \lambda_c > \lambda_{lim} \quad (13)$$

$$\lambda_c = \sqrt{F_y/F_{cr}} \quad (14)$$

where F_{cr} = elastic flexural buckling stress; $\alpha = 1.38$; $\beta_0 = 0.38$; $\beta_1 = 0.5$; $\beta_2 = 0.82$; and $\lambda_{lim} = 1.79$ for austenitic and duplex rectangular HSS. It is worth noting that the transition slenderness λ_{lim} was defined under the assumption that both stainless steel families had the

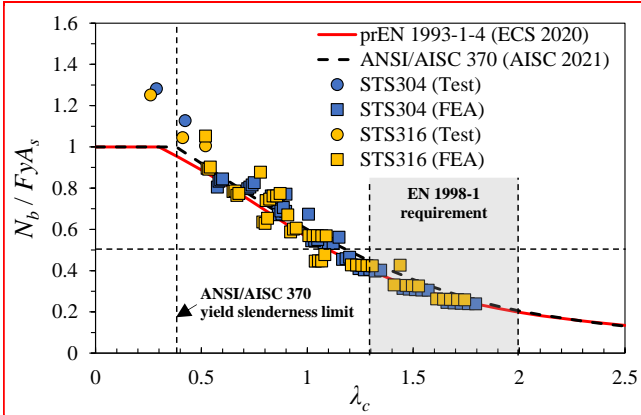


Fig. 8 Material properties assigned in SHS brace FE model

proportionality limit around 30% of F_y . The applicability of the European and American buckling curves for SHS braces subjected to cyclic loading are examined on the basis of the test and FEA data as shown in Fig. 8, where the buckling strengths N_b normalised by the cross-sectional squash load $F_y A_s$ are plotted against the global slenderness.

As suggested in previous studies (Ma et al. 2018; Tayyebi & Sun 2021), the yield stress of flat region material was used to derive the squash load. The results indicate that both buckling curves, which is developed based on the results of columns under static compressive loading, can predict the flexural buckling strengths of stainless steel SHS brace specimens tested under cyclic loading with high accuracy.

The statistical evaluation of design codes is presented in Table 7, indicating that the European buckling curve provides a slightly more accurate and less scattered predictions for all tested specimens, regardless of stainless steel material types. It can be also seen from Fig. 8 that the yield slenderness limit prescribed in AISC 370 ($\lambda_c = 0.38$) is appropriate for the STS316 specimens, while the prEN1993-1-4 limit ($\lambda_c = 0.3$) is conservative.

According to the European code for earthquake resistant design (Eurocode 2013) deriving from result of carbon steel cyclic test, SHS braces should be designed to have the global

slenderness larger than 1.3 to ensure $N_b < 0.5F_y A_s$ to overloading the column (Metelli 2013; Trutalli et al. 2019). However, this condition is inconsistent with the present FE results, in which when $\lambda_c = 1.2$, the buckling strength is about 45%.

4.2 Post-buckling strength

According to the AISC 341-16 seismic provisions for Structural Steel buildings (AISC 2016), connections, beams, and columns in CBFs should be designed to develop the post-buckling strength of the braces, which is expected to be 30% of the initial buckling strength N_b , regardless of ductility level. In contrast, Tremblay (2013) proposed empirical equation for the minimum post-buckling strength of carbon steel brace members at various ductility levels ($2\Delta_y$, $3\Delta_y$ and $5\Delta_y$).

The normalised post-buckling strengths at displacement of $2\Delta_y$ and $4\Delta_y$ are compared with those post-buckling models, as shown in Fig. 9, where the linear interpolation method is used for ductility level of $4\Delta_y$. It can be seen that Tremblay’s model (2013) provides more accurate predictions for post-buckling strength at $2\Delta_y$ in comparison to the AISC curve, which yield consistently too conservative predictions. However, for post buckling strength at $4\Delta_y$, a significant number of test and FEA data lies below the AISC curves, and Tremblay’s model (2013) is no longer valid. It should be noted that the model was found to be accurate for cold-formed austenitic stainless steel specimens of Nip et al. (2010a).

4.3 Prediction of ductility capacity

The ductility capacity of the tested cold-formed stainless steel SHS brace specimens have been quantified, which is an important parameter to ensure desirable seismic performance of the structures. AISC 341-16 seismic provision (AISC 2016) prescribes stringent limit for width-to-thickness ratio of HSS braces in CBFs, as given in Eqs. (15) and (16). This is to reduce the likelihood of immature fracture arising from

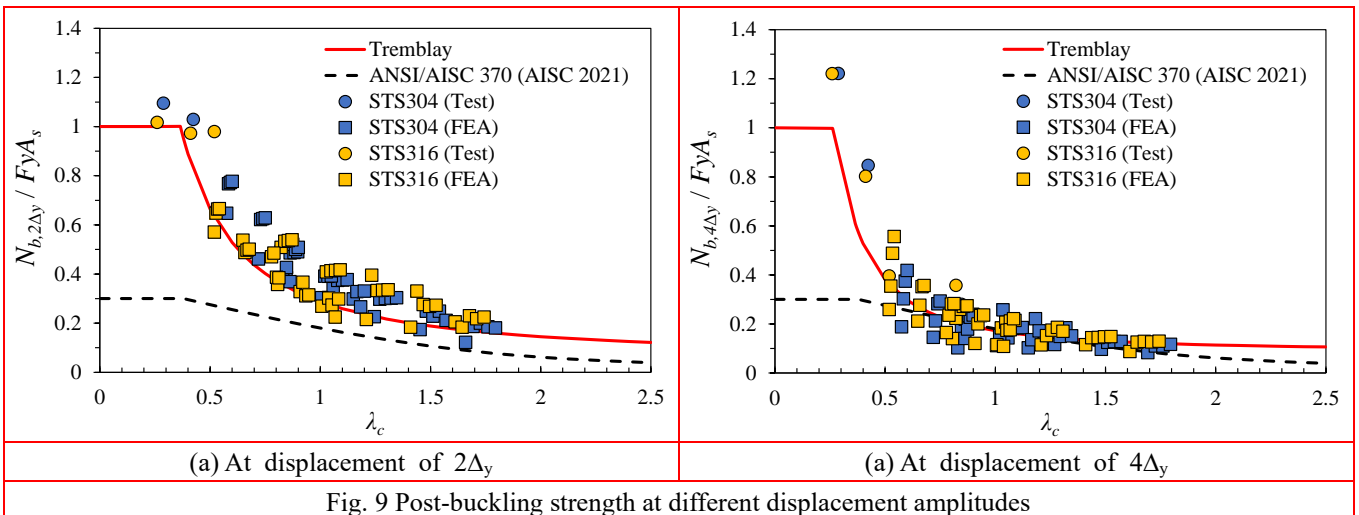
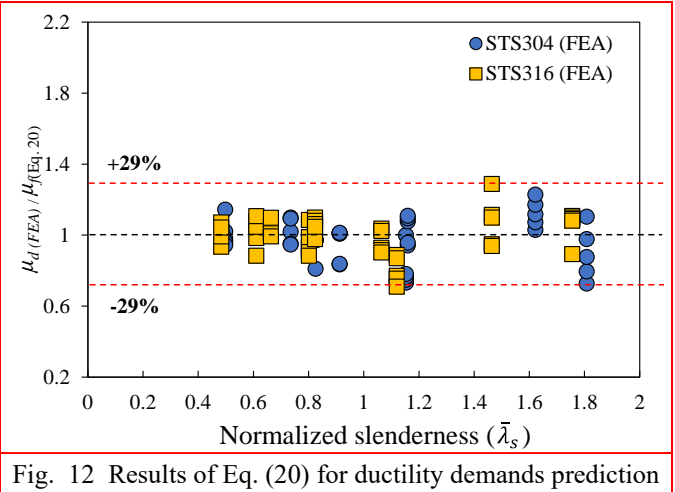
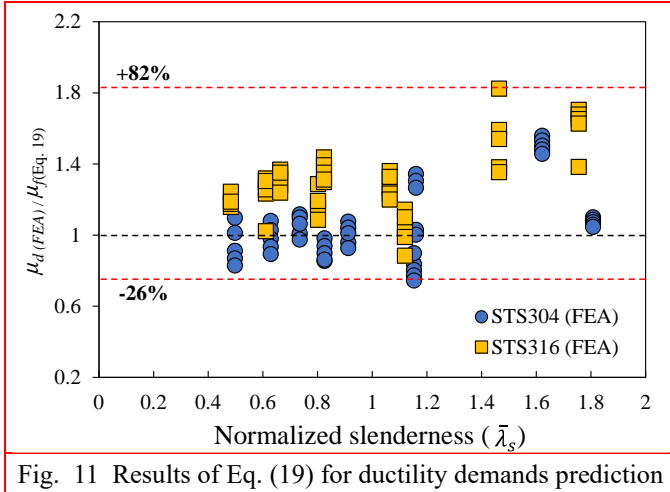


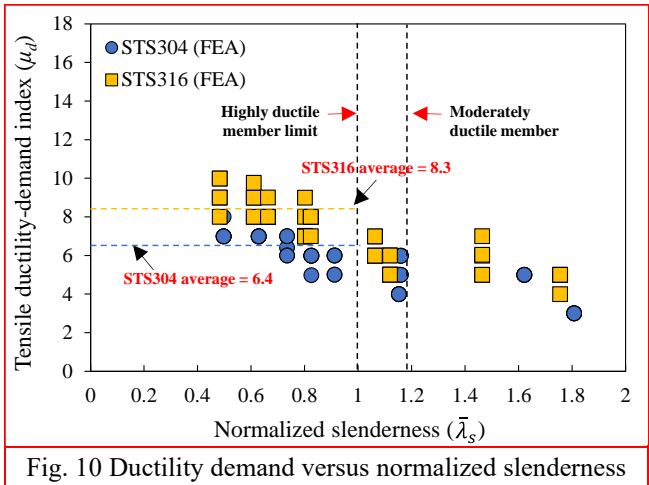
Fig. 9 Post-buckling strength at different displacement amplitudes



is to reduce the likelihood of immature fracture arising from the local buckling.

$\lambda_{hd} = 0.65 \sqrt{\frac{E}{R_y F_y}}$ for highly-ductile members	(15)
$\lambda_{md} = 0.76 \sqrt{\frac{E}{R_y F_y}}$ for moderately-ductile members	(16)

where R_y = ratio of the expected yield stress to the specified minimum yield stress, which is taken as 1.0 herein.



As seen in Fig. 10, the tensile ductility-demand prior to fracture increases with decreases in $\bar{\lambda}_s$. The discrepancy in the ductility capacity between STS304 and STS316 specimens is more noticeable in highly ductile members ($\bar{\lambda}_s \leq 1.0$) in AISC 341-16 (AISC 2016), rather than moderately ductile members ($1.0 < \bar{\lambda}_s \leq 1.17$). The STS316 highly ductile specimens possessed approximately 30% ($8.3/6.4=1.30$) higher ductility capacity on average than the comparable STS304 specimens, which is consistent the test results reported by Kim et al. (2021).

Based on the laboratory test results from nine cold-formed stainless HSS braces, Nip et al. (2010a) proposed a fracture model for prediction of the tensile ductility-demand as follows:

$\mu_f = -3.42 + 19.86\lambda_c + 0.21\lambda_s - 0.64\lambda_c\lambda_s$	(19)
---	------

Fig. 11 presents comparison of the predicted ductility-demand by Eq. (19) $\mu_{f(Eq. 19)}$ with those obtained in the FE analysis. It is evident that the model proposed by Nip et al. (2010a) yield unsafe predictions for a large number of the STS304 specimens, and also result in high level of conservatism for the STS 316 specimens. This implies that due account needs to be taken to consider the difference of stainless steel grades in the model. The model coefficients in Eq. (19) were optimized to suit the test and FE results of austenitic stainless steel SHS brace specimens, as given in Eq. (20).

$\mu_f = 6.59 + 1.50\lambda_c - 0.03\lambda_s - 0.09\lambda_c\lambda_s$	(20a)
for STS304 stainless steel	
$\mu_f = 8.76 + 1.55\lambda_c - 0.13\lambda_s - 0.04\lambda_c\lambda_s$	(20b)
for STS316 stainless steel	

The normalized slenderness $\bar{\lambda}_s$ was introduced to ensure a consistent comparison between the different steel materials and sections, as defined by Eq. (17). A tensile ductility-demand index μ_d , defined as the ratio of the maximum tensile deformation Δ_t to the yield deformation Δ_y , was also used.

$\bar{\lambda}_s = \frac{b/t}{\lambda_{hd}}$	(17)
$\mu_d = \frac{\Delta_t}{\Delta_y}$	(18)

Comparisons of the modified model for ductility prediction $\mu_{d(FEA)}/\mu_f$ are illustrated in Fig. 12, and quantified in terms of mean and COV values in Table 8. It can be seen that the optimized coefficient in Eq. (20) significantly improves the accuracy and consistency of the equation in predicting ductility-demand of the examined specimens.

Table 8 Comparison of FEA results with predicted ductility-demand

No. of FEA: 90	$\mu_{d(FEA)}/\mu_f$	
	Eq. (19)	Eq. (20)
Mean	1.18	0.99
COV	0.164	0.109

5. Conclusions

A comprehensive finite element modelling procedures for cold-formed austenitic stainless SHS braces under cyclic axial loading has been described in this research, with aims to produce reliable numerical data with high efficiency. A ductile fracture model was incorporated into FE model to replicate the material softening and the damage accumulation, which enables prediction of fracture life. The developed finite element models were validated with their counterpart laboratory test results reported by the corresponding author (Kim et al. 2021). The models were further employed to perform parametric studies to examine applicability range of the predictive models available in national design codes and in the literature for initial/post buckling strengths and fracture life. Based on the FEA results, the following conclusions can be drawn:

- Hysteretic behavior of cold-formed austenitic stainless SHS braces was replicated with FE models incorporating the combined isotropic/kinematic hardening rule and the Void Growth Model (VGM) criterion. The FEA results exhibited satisfactory agreement with the test results with respect to the initial buckling strength. The average difference is around 1% for seven brace specimens having different global slenderness and the local slenderness. VGM was found to be accurate in predicting fracture initiation and propagation at the mid-span of braces.
- The accuracy of buckling curves specified in the European and the American design codes were examined. Although the design curves were derived from results of quasi-static laboratory tests, it shows good predictions for initial buckling strengths of the SHS braces subjected to cyclic loading. The European buckling curve was found to estimate better prediction than the American one, but their yield slenderness limit is too conservative. The lower limit of global slenderness imposed by the European seismic design code was evaluated. It was found that the global slenderness limit can be reduced up to 1.2 for cold-formed stainless steel SHS braces.
- Tremblay's model, which is developed on the results of carbon steel specimens was found to be applicable for the post-buckling strength of stainless steel specimens at displacement of $2\Delta_y$, but inaccurate for many specimens at displacement of $4\Delta_y$. On the other hand, the American seismic

design guideline provided consistently inaccurate predictions for both $2\Delta_y$ and $4\Delta_y$.

- Fracture life of the brace specimens was quantified using a tensile ductility-demand index. For members with moderately ductile level according to AISC 341-16, the STS 316 specimens had comparable ductility demand prior to fracture with the STS 304 one. However, noticeable difference was observed in the brace specimens with highly ductile level, in which the STS 316 specimens had 30% greater ductility demand.
- The empirical equation proposed by Nip et al. was found to provide significantly inaccurate and scattered predictions for ductility demand-index of stainless steel SHS brace specimens tested in the present work. The modified equation was proposed by considering the difference of stainless steel material with optimized model coefficients. The modified predictive model exhibited significantly improved accuracy and consistency, with a mean FE-to-predicted ratio of 0.99 with associated COV of 0.109.

Acknowledgments

The first author is supported by Basic Science Research through the National Research Foundation of Korea (NRF) funded by the Ministry of Education (2021R111A1A01059354). The last author is supported by Basic Science Research through the National Research Foundation of Korea (NRF) funded by the Ministry of Education (No. NRF2018R1D1A1B07046021).

References

- ABAQUS, ABAQUS Analysis User's Manual, Dassault Systemes Simulia Corporation; Providence, RI, USA.
- Ahmed, S. and Ashraf, M. (2017), "Numerical investigation on buckling resistance of stainless steel hollow members", *J. Construct. Steel Res.*, **136**, 193-203. <https://doi.org/10.1016/j.jcsr.2004.06.001>.
- Ashraf, M., Gardner, L. and Nethercot, D.A. (2005), "Strength enhancement of the corner regions of stainless steel cross-sections", *J. Construct. Steel Res.*, **61**(1), 37-52. <https://doi.org/10.1016/j.jcsr.2004.06.001>.
- Ashraf, M., Gardner, L. and Nethercot, D.A. (2006), "Finite element modelling of structural steel cross-sections", *Thin-Walled Struct.*, **44**(10), 1048-1062. <https://doi.org/10.1016/j.tws.2006.10.010>.
- AISC ANSI/AISC 341-16 (2016), Seismic provisions for structural steel buildings, American Institute of Steel Construction; Chicago, IL, USA.
- AISC ANSI/AISC 370-21 (2021), Specification for structural stainless steel buildings, American Institute of Steel Construction; Chicago, IL, USA.
- AISI (1968), Specification for the design of light gage cold-formed stainless steel structural members, American Iron and Steel Institute; New York, NY, USA.
- ASTM E8-16 (2016), Standard Test Methods for Tension Testing of metallic Materials, ASTM International; West Conshohocken,

PA, USA.

- ATC-24 (1992), Guidelines for cyclic seismic testing of components of steel structures for building, Applied Technology Council; Redwood City, CA, USA.
- Chiu, P.K., Weng, K.L., Wang, S.H., Yang, J.R., Huang, Y.S. and Fang, J. (2005), "Low-cycle fatigue-induced martensitic transformation in SAF 220 duplex stainless steel", *Mater. Sci. Eng. A.*, **398**(1-2), 349-359.
<https://doi.org/10.1016/j.msea.2005.03.096>.
- Eurocode (2015), Design of Steel Structures. Part 1.4: General rules. Supplementary rules for stainless steels, European Committee for Standardisation; Brussels, Belgium.
- Eurocode (2020), Design of Steel Structures. Part 1.4: General rules. Supplementary rules for stainless steels, European Committee for Standardisation; Brussels, Belgium.
- Eurocode (2013), Design of Structures for Earthquake resistance. Part 1: General rules. Seismic actions and rules for buildings, European Committee for Standardisation; Brussels, Belgium.
- Fang, C., Zhou, F. and Luo, C. (2018), "Cold-formed stainless steel RHSs/SHSs under combined compression and cyclic bending", *J. Construct. Steel Res.*, **141**, 9-22.
<https://doi.org/10.1016/j.jcsr.2017.11.001>.
- Haddad, M. (2015), "Concentric tubular steel braces subjected to seismic loading: Finite element modeling", *J. Construct. Steel Res.*, **104**, 155-166.
<https://doi.org/10.1016/j.jcsr.2014.10.013>.
- Hassan, M.S, Salawdeh, S. and Goggins, J. (2018), "Determination of geometrical imperfection models in finite element analysis of structural steel hollow sections under cyclic axial loading", *J. Construct. Steel Res.*, **141**, 189-203.
<https://doi.org/10.1016/j.jcsr.2017.11.012>.
- Kim, R.H., Kim, T.S., Im, S.H. and Xi, Y. (2021), "Hysteretic behavior comparison of austenitic and lean duplex stainless steel square hollow section members under cyclic axial loading", *Eng. Struct.*, **237**(15), 112227.
<https://doi.org/10.1016/j.engstruct.2021.112227>.
- KS KS D 3536 (2015), Stainless steel pipes for machine and structural purpose, Korean Industrial Standards; Seoul, Korea.
- Kumar, A.P.C. and Shaoo, D.R. (2018), "Fracture ductility of hollow circular and square steel braces under cyclic loading", *Thin-Walled Struct.*, **130**, 347-361.
<https://doi.org/10.1016/j.tws.2018.06.005>.
- Lemaitre, J. and Chaboche, J.L. (1994), "Mechanics of solid materials", Cambridge University Press; Cambridge, UK.
<https://doi.org/10.1017/CBO9891139167970>.
- Liu, Y. and Young, B. (2003), "Buckling of stainless steel square hollow section compression members", *J. Construct. Steel Res.*, **59**(2), 165-177.
[https://doi.org/10.1016/S0143-974X\(02\)00031-7](https://doi.org/10.1016/S0143-974X(02)00031-7).
- Ma, J.L., Chan, T.M. and Young, B. (2018), "Design of cold-formed high-strength steel tubular stub columns", *J. Struct. Eng.*, **144**, 04018063.
[https://doi.org/10.1061/\(ASCE\)ST.1943-541X.0002046](https://doi.org/10.1061/(ASCE)ST.1943-541X.0002046).
- Metelli, G. (2013), "Theoretical and experimental study on the cyclic behaviour of X braced steel frames", *Eng. Struct.*, **46**, 763-773.
<https://doi.org/10.1016/j.engstruct.2012.08.021>.
- Nip, K.H., Gardner, L. and Elghazouli, A.Y. (2010a), "Cyclic testing and numerical modelling of carbon steel and stainless steel tubular bracing members", *Eng. Struct.*, **32**(2), 424-441.
<https://doi.org/10.1016/j.engstruct.2009.10.005>.
- Nip, K.H., Gardner, L., Davies, C.M. and Elghazouli, A.Y. (2010b), "Extremely low cycle fatigue tests on structural carbon steel and stainless steel", *J. Construct. Steel Res.*, **66**(1), 96-110.
<https://doi.org/10.1016/j.jcsr.2009.08.004>.
- Rice, J.R. and Tracey, D.M. (1969), "On the ductile enlargement of voids in triaxial stress fields", *J. Mech. Phys. Solids*, **17**(3), 201-217.
[https://doi.org/10.1016/0022-5096\(69\)90033-7](https://doi.org/10.1016/0022-5096(69)90033-7).
- Shrinivas, V., Varma, S.K. and Murr, L.E. (1995), "Deformation-induced martensitic characteristics in 304 and 316 stainless steels during room-temperature rolling", *Metall. Mater. Trans. A.*, **26**(3), 661-671.
<https://doi.org/10.1007/BF02663916>.
- Sohrabi, M.J., Naghizadeh, M. and Hamed, M. (2020), "Deformation-induced martensite in austenitic stainless steels: A review", *Arch. Civ. Mech. Eng.*, **20**(4), 1-24.
<https://doi.org/10.1007/s43452-020-00130-1>.
- Tayyebi, K. and Sun, M. (2021), "Design of direct-formed square and rectangular hollow section stub columns", *J. Construct. Steel Res.*, **178**, 16499.
<https://doi.org/10.1016/j.jcsr.2020.106499>.
- Tremblay, R. (2002), "Inelastic seismic response of steel bracing members", *J. Construct. Steel Res.*, **58**(5-8), 665-701.
[https://doi.org/10.1016/S0143-974X\(01\)00104-3](https://doi.org/10.1016/S0143-974X(01)00104-3).
- Trutalli, D., Stefani, L.D., Marchi, L. and Scotta, R. (2019), "Seismic capacity of steel frames braced with cross-concentric rectangular plates: Non-linear analyses", *J. Construct. Steel Res.*, **161**, 128-136.
<https://doi.org/10.1016/j.jcsr.2019.07.003>.
- Wang, F., Young, B. and Gardner, L. (2020), "Compressive behaviour and design of CFDST cross sections with stainless steel outer tubes", *J. Construct. Steel Res.*, **170**, 105942.
<https://doi.org/10.1016/j.jcsr.2020.105942>.
- Yang, F., Veljkovic, M. and Liu, Y. (2021), "Fracture simulation of partially threaded bolts under tensile loading", *Eng. Struct.*, **226**, 111373.
<https://doi.org/10.1016/j.engstruct.2020.111373>.
- Zheng, S., Zhou, F., Cheng, J., Li, H.T. and Rong, R. (2022), "Experimental study on cyclic hardening characteristics of structural stainless steels", *J. Construct. Steel Res.*, **191**, 107196.
<https://doi.org/10.1016/j.jcsr.2022.107196>.
- Zhou, F., Fang, C. and Chen, Y. (2018), "Experimental and numerical studies on stainless steel tubular members under axial cyclic loading", *Eng. Struct.*, **171**(15), 72-85.
<https://doi.org/10.1016/j.engstruct.2018.05.093>.
- Zhou, F., Huang, L. and Li, H.T. (2022), "Cold-formed stainless steel SHS and RHS columns subjected to local flexural interactive buckling", *J. Construct. Steel Res.*, **188**, 106999.
<https://doi.org/10.1016/j.engstruct.2018.05.093>.
- Zub, C.I., Stratan, A. and Dubina, D. (2019), "Calibration of parameters of combined hardening model using tensile tests", *SDSS 2019 – International Colloquium on Stability and Ductility of Steel Structures*.